Biomedical Optics EXPRESS

Single input state polarization sensitive swept source optical coherence tomography based on an all single mode fiber interferometer

Wolfgang Trasischker,* Stefan Zotter, Teresa Torzicky, Bernhard Baumann, Richard Haindl, Michael Pircher, and Christoph K. Hitzenberger

Center for Medical Physics and Biomedical Engineering, Medical University of Vienna, Waehringer Guertel 18-20, 4L, A-1090 Vienna, Austria

wolfgang.trasischker@meduniwien.ac.at

Abstract: We present a newly developed single mode fiber based swept source polarization sensitive optical coherence tomography system using a single input state at 1040 nm. Two non-polarizing fiber based beam splitters are combined to form a Mach-Zehnder interferometer, while two polarizing beam splitters are used to obtain a polarization sensitive detection. Both types of beam splitters solely feature conventional single mode fibers. Polarization control paddles are used to set and maintain the polarization states in the fibers of the interferometer and detection unit. By use of a special paddle alignment scheme we are able to eliminate any bulk optic wave plates and polarization maintaining fibers in the interferometer and detection paths while preserving the advantages of a single input state system that illuminates the sample with circularly polarized light. To demonstrate the capabilities of our system, we performed retinal measurements on healthy human volunteers.

OCIS codes: (170.0170) Medical optics and biotechnology; (170.0110) Imaging systems; (170.2655) Functional monitoring and imaging; (170.4500) Optical coherence tomography; (170.4470) Ophthalmology; (060.2430) Fibers, single-mode

References and links

1. D. Huang, E. A. Swanson, C. P. Lin, J. S. Schuman, W. G. Stinson, W. Chang, M. R. Hee, T. Flotte, K. Gregory, C. A. Puliafito, and J. G. Fujimoto, "Optical coherence tomography," Science **254**(5035), 1178–1181 (1991).
2. A. F. Fercher, W. Drexler, C. K. Hitzenberger, and T. Lasser, "Optical coherence tomography - principles and applications," Rep. Prog. Phys. **66**(2), 239–303 (2003).
3. D. Stifter, "Beyond biomedicine: a review of alternative applications and developments for optical coherence tomography," Appl. Phys. B **88**(3), 337–357 (2007).
4. S. Marschall, B. Sander, M. Mogensen, T. M. Jørgensen, and P. E. Andersen, "Optical coherence tomography-current technology and applications in clinical and biomedical research," Anal. Bioanal. Chem. **400**(9), 2699–2720 (2011).
5. W. Drexler and J. G. Fujimoto, "State-of-the-art retinal optical coherence tomography," Prog. Retin. Eye Res. **27**(1), 45–88 (2008).
6. R. Leitgeb, C. K. Hitzenberger, and A. F. Fercher, "Performance of fourier domain vs. time domain optical coherence tomography," Opt. Express **11**(8), 889–894 (2003).
7. J. F. de Boer, B. Cense, B. H. Park, M. C. Pierce, G. J. Tearney, and B. E. Bouma, "Improved signal-to-noise ratio in spectral-domain compared with time-domain optical coherence tomography," Opt. Lett. **28**(21), 2067–2069 (2003).
8. M. Choma, M. Sarunic, C. Yang, and J. Izatt, "Sensitivity advantage of swept source and Fourier domain optical coherence tomography," Opt. Express **11**(18), 2183–2189 (2003).
9. A. F. Fercher, C. K. Hitzenberger, G. Kamp, and S. Y. Elzaiat, "Measurement of intraocular distances by backscattering spectral interferometry," Opt. Commun. **117**(1-2), 43–48 (1995).
10. S. R. Chinn, E. A. Swanson, and J. G. Fujimoto, "Optical coherence tomography using a frequency-tunable optical source," Opt. Lett. **22**(5), 340–342 (1997).
11. T. Klein, W. Wieser, L. Reznicek, A. Neubauer, A. Kampik, and R. Huber, "Multi-MHz retinal OCT," Biomed. Opt. Express **4**(10), 1890–1908 (2013).
12. A. Unterhuber, B. Povazay, B. Hermann, H. Sattmann, A. Chavez-Pirson, and W. Drexler, "In vivo retinal optical coherence tomography at 1040 nm - enhanced penetration into the choroid," Opt. Express **13**(9), 3252–3258 (2005).

#210928 - $15.00 USD Received 2 May 2014; revised 24 Jun 2014; accepted 18 Jul 2014; published 28 Jul 2014

13. X. J. Wang, T. E. Milner, and J. S. Nelson, "Characterization of fluid flow velocity by optical Doppler tomography," Opt. Lett. **20**(11), 1337–1339 (1995).
14. Z. P. Chen, T. E. Milner, D. Dave, and J. S. Nelson, "Optical Doppler tomographic imaging of fluid flow velocity in highly scattering media," Opt. Lett. **22**(1), 64–66 (1997).
15. J. A. Izatt, M. D. Kulkarni, S. Yazdanfar, J. K. Barton, and A. J. Welch, "In vivo bidirectional color Doppler flow imaging of picoliter blood volumes using optical coherence tomography," Opt. Lett. **22**(18), 1439–1441 (1997).
16. M. R. Hee, D. Huang, E. A. Swanson, and J. G. Fujimoto, "Polarization-sensitive low-coherence reflectometer for birefringence characterization and ranging," J. Opt. Soc. Am. B **9**(6), 903–908 (1992).
17. J. F. de Boer, T. E. Milner, M. J. C. van Gemert, and J. S. Nelson, "Two-dimensional birefringence imaging in biological tissue by polarization-sensitive optical coherence tomography," Opt. Lett. **22**(12), 934–936 (1997).
18. C. K. Hitzenberger, E. Goetzinger, M. Sticker, M. Pircher, and A. Fercher, "Measurement and imaging of birefringence and optic axis orientation by phase resolved polarization sensitive optical coherence tomography," Opt. Express **9**(13), 780–790 (2001).
19. M. Pircher, C. K. Hitzenberger, and U. Schmidt-Erfurth, "Polarization sensitive optical coherence tomography in the human eye," Prog. Retin. Eye Res. **30**(6), 431–451 (2011).
20. B. Thylefors, A. D. Négrel, R. Pararajasegaram, and K. Y. Dadzie, "Global data on blindness," Bull. World Health Organ. **73**(1), 115–121 (1995).
21. R. R. A. Bourne, G. A. Stevens, R. A. White, J. L. Smith, S. R. Flaxman, H. Price, J. B. Jonas, J. Keeffe, J. Leasher, K. Naidoo, K. Pesudovs, S. Resnikoff, and H. R. Taylor, "Causes of vision loss worldwide, 1990 –2010: a systematic analysis," Lancet Glob. Health **1**(6), 339–349 (2013).
22. A. W. Dreher, K. Reiter, and R. N. Weinreb, "Spatially resolved birefringence of the retinal nerve fiber layer assessed with a retinal laser ellipsometer," Appl. Opt. **31**(19), 3730–3735 (1992).
23. B. Cense, T. C. Chen, B. H. Park, M. C. Pierce, and J. F. de Boer, "Invivo depth-resolved birefringence measurements of the human retinal nerve fiber layer by polarization-sensitive optical coherence tomography," Opt. Lett. **27**(18), 1610–1612 (2002).
24. M. Yamanari, M. Miura, S. Makita, T. Yatagai, and Y. Yasuno, "Phase retardation measurement of retinal nerve fiber layer by polarization-sensitive spectral-domain optical coherence tomography and scanning laser polarimetry," J. Biomed. Opt. **13**(1), 014013 (2008).
25. B. Baumann, S. O. Baumann, T. Konegger, M. Pircher, E. Götzinger, F. Schlanitz, C. Schütze, H. Sattmann, M. Litschauer, U. Schmidt-Erfurth, and C. K. Hitzenberger, "Polarization sensitive optical coherence tomography of melanin provides intrinsic contrast based on depolarization," Biomed. Opt. Express **3**(7), 1670–1683 (2012).
26. E. Götzinger, M. Pircher, W. Geitzenauer, C. Ahlers, B. Baumann, S. Michels, U. Schmidt-Erfurth, and C. K. Hitzenberger, "Retinal pigment epithelium segmentation by polarization sensitive optical coherence tomography," Opt. Express **16**(21), 16410–16422 (2008).
27. F. G. Schlanitz, B. Baumann, T. Spalek, C. Schütze, C. Ahlers, M. Pircher, E. Götzinger, C. K. Hitzenberger, and U. Schmidt-Erfurth, "Performance of Automated Drusen Detection by Polarization-Sensitive Optical Coherence Tomography," Invest. Ophthalmol. Vis. Sci. **52**(7), 4571–4579 (2011).
28. C. Schütze, M. Bolz, R. Sayegh, B. Baumann, M. Pircher, E. Götzinger, C. K. Hitzenberger, and U. Schmidt-Erfurth, "Lesion Size Detection in Geographic Atrophy by Polarization-Sensitive Optical Coherence Tomography and Correlation to Conventional Imaging Techniques," Invest. Ophthalmol. Vis. Sci. **54**(1), 739–745 (2013).
29. C. E. Saxer, J. F. de Boer, B. H. Park, Y. Zhao, Z. Chen, and J. S. Nelson, "High-speed fiber based polarization-sensitive optical coherence tomography of in vivo human skin," Opt. Lett. **25**(18), 1355–1357 (2000).
30. E. Götzinger, B. Baumann, M. Pircher, and C. K. Hitzenberger, "Polarization maintaining fiber based ultra-high resolution spectral domain polarization sensitive optical coherence tomography," Opt. Express **17**(25), 22704–22717 (2009).
31. D. P. Davé, T. Akkin, and T. E. Milner, "Polarization-maintaining fiber-based optical low-coherence reflectometer for characterization and ranging of birefringence," Opt. Lett. **28**(19), 1775–1777 (2003).
32. B. Park, M. C. Pierce, B. Cense, S.-H. Yun, M. Mujat, G. Tearney, B. Bouma, and J. de Boer, "Real-time fiber-based multi-functional spectral-domain optical coherence tomography at 1.3 microm," Opt. Express **13**(11), 3931–3944 (2005).
33. W. Y. Oh, S. H. Yun, B. J. Vakoc, M. Shishkov, A. E. Desjardins, B. H. Park, J. F. de Boer, G. J. Tearney, and B. E. Bouma, "High-speed polarization sensitive optical frequency domain imaging with frequency multiplexing," Opt. Express **16**(2), 1096–1103 (2008).
34. M. Yamanari, S. Makita, and Y. Yasuno, "Polarization-sensitive swept-source optical coherence tomography with continuous source polarization modulation," Opt. Express **16**(8), 5892–5906 (2008).
35. H. Lin, M.-C. Kao, C.-M. Lai, J.-C. Huang, and W.-C. Kuo, "All fiber optics circular-state swept source polarization-sensitive optical coherence tomography," J. Biomed. Opt. **19**(2), 021110 (2014).
36. E. Götzinger, M. Pircher, and C. K. Hitzenberger, "High speed spectral domain polarization sensitive optical coherence tomography of the human retina," Opt. Express **13**(25), 10217–10229 (2005).
37. S. Zotter, M. Pircher, T. Torzicky, B. Baumann, H. Yoshida, F. Hirose, P. Roberts, M. Ritter, C. Schütze, E. Götzinger, W. Trasischker, C. Vass, U. Schmidt-Erfurth, and C. K. Hitzenberger, "Large-field high-speed polarization sensitive spectral domain OCT and its applications in ophthalmology," Biomed. Opt. Express **3**(11), 2720–2732 (2012).
38. T. Torzicky, M. Pircher, S. Zotter, M. Bonesi, E. Götzinger, and C. K. Hitzenberger, "High-Speed Retinal Imaging with Polarization-Sensitive OCT at 1040 nm," Optom. Vis. Sci. **89**(5), 585–592 (2012).

#210928 - $15.00 USD Received 2 May 2014; revised 24 Jun 2014; accepted 18 Jul 2014; published 28 Jul 2014

39. M. Pircher, E. Götzinger, B. Baumann, and C. K. Hitzenberger, "Corneal birefringence compensation for polarization sensitive optical coherence tomography of the human retina," J. Biomed. Opt. **12**(4), 041210 (2007).
40. American National Standards for safe use of lasers," in ANSI Z 136.1, A. N. S. Institute, Ed., Laser Institute of America, Orlando (2000).
41. Safety of laser products - Part 1: Equipment classification and requirements," in IEC 60825–1 Ed. 2, I. E. Commission, Ed., International Electrotechnical Commission, Geneva (2001).
42. B. Cense, Q. Wang, S. Lee, L. Zhao, A. E. Elsner, C. K. Hitzenberger, and D. T. Miller, "Henle fiber layer phase retardation measured with polarization-sensitive optical coherence tomography," Biomed. Opt. Express **4**(11), 2296–2306 (2013).
43. B. Cense, T. C. Chen, B. H. Park, M. C. Pierce, and J. F. de Boer, "Thickness and birefringence of healthy retinal nerve fiber layer tissue measured with polarization-sensitive optical coherence tomography," Invest. Ophthalmol. Vis. Sci. **45**(8), 2606–2612 (2004).
44. B. Baumann, C. Schütze, C. K. Hitzenberger, F. Schlanitz, E. Götzinger, M. Pircher, C. Ahlers, U. Schmidt-Erfurth, and H. Sattmann, "Segmentation and quantification of retinal lesions in age-related macular degeneration using polarization-sensitive optical coherence tomography," J. Biomed. Opt. **15**, 061704 (2010).
45. M. Pircher, E. Götzinger, R. Leitgeb, H. Sattmann, O. Findl, and C. Hitzenberger, "Imaging of polarization properties of human retina in vivo with phase resolved transversal PS-OCT," Opt. Express **12**(24), 5940–5951 (2004).
46. R. W. Knighton, X.-R. Huang, and D. S. Greenfield, "Analytical Model of Scanning Laser Polarimetry for Retinal Nerve Fiber Layer Assessment," Invest. Ophthalmol. Vis. Sci. **43**(2), 383–392 (2002).

1. Introduction

Developed more than two decades ago OCT is nowadays widely used in medical research, diagnostics and many other fields [1–4]. Due to its ability to non-invasively provide high resolution cross-sectional data at short acquisition times, OCT is best suited for in vivo imaging. The combination of these characteristics with the transparency of ocular media, as well as its thin layer composition, paved the way to OCT's most prominent applications in ophthalmology [5]. Until today, the initially developed time domain OCT technique was almost entirely replaced by Fourier domain (FD) techniques, mainly due to sensitivity and imaging speed advantages [6–8]. Nowadays two different FD-OCT techniques, spectral domain (SD) [9] and swept source OCT (SS-OCT) [10] are used. While the first approach uses a broadband light source and a spectrometer in the detection unit, the latter features a tunable light source in combination with a point detector. In general SS-OCT is associated with a higher imaging speed, currently being up to 10 times faster than SD-OCT [11].

Driven by its use in ophthalmology and the available light sources, the commercially available OCT devices mainly feature light in the 840 nm regime. In recent years other wavelength ranges gained more and more interest in research. Due to the water absorption minimum, lower scattering and therefore deeper tissue penetration the use of light centered around 1050 nm showed promising results especially in retinal imaging [12].

After its introduction OCT was not only further developed in terms of imaging speed and sensitivity but also functional extensions were developed. Modalities like Doppler-OCT, which targets information on the movement of backscattering particles [13–15], or polarization sensitive OCT (PS-OCT) [16–18], provide additional image contrast. The latter measures alterations of the polarization state of the light induced by the sample. In biological samples light-tissue interactions like birefringence and depolarization are responsible for changes of the polarization state [19]. This enables to distinguish polarization preserving, birefringent and depolarizing tissue by a polarization sensitive detection.

In recent years PS-OCT showed promising results in diagnosing ocular diseases which involve tissue that changes the polarization state of the probing light. Especially in glaucoma and age related macular degeneration (AMD), PS-OCT can provide important information. Both of the mentioned diseases are leading causes of blindness worldwide [20,21].

The retinal nerve fiber layer (RNFL) is a birefringent layer of the retina [22]. During the progression of glaucoma, the ganglion cell axons degrade, leading to a thinning of the RNFL, to visual field defects, or even blindness. One measure for RNFL degradation is via its birefringence: The reduced RNFL thickness leads to reduced retardation between orthogonal polarization states, and by using PS-OCT this effect can be observed in depth resolved manner [23,24].

#210928 - $15.00 USD Received 2 May 2014; revised 24 Jun 2014; accepted 18 Jul 2014; published 28 Jul 2014

As has been shown, the retinal pigment epithelium (RPE) has depolarizing properties, most likely due to its melanin content [25]. This characteristic can be used to segment this layer using PS-OCT [26] and provide a means of quantitative evaluation of RPE lesions that frequently occur in AMD like drusen [27] and geographic atrophies [28].

Various schemes of FD PS-OCT setups were developed in the past [16,18,29,30]. Using bulk optics, the sample can be illuminated by a well-defined polarization state while the state is maintained throughout the setup. For the case of fiber based techniques polarization maintaining (PM) fibers can avoid unwanted polarization state transformations [31]. This provides a robust OCT setup with little alignment effort. However, cross coupling between the polarization channels at fiber connectors and splices can introduce ghost images and other artefacts [30,31]. These effects arise due to the refractive index difference for the orthogonal polarization modes traveling in the fiber. Primary image and ghost can be separated in depth by using long PM fibers after the leaking position. This shifts the ghost to a position where it does not influence the measurement. However, this increases the complexity of such a system. The use of normal single mode (SM) instead of PM fibers avoids these problems, however, implies that the polarization state of the light is not maintained. This can lead to unknown polarization states at the sample and along the fiber based system. PS-OCT techniques that probe the sample with different input polarization states, either by sequential illumination [29,32] or multiplexing [33,34] can circumvent the necessity of a predefined polarization state at the sample. Although these approaches enable the application of normal SM fibers, their use is traded for increased system complexity and a slower data acquisition or limited imaging depth.

Using conventional SM fibers in combination with a single, predefined polarization state would reduce system complexity, ghosts and could decrease the fiber length without sacrificing acquisition speed or image depth. A hybrid PM/SM fiber based system, using a predefined sampling beam polarization state, has been reported [35]. Furthermore, an SM fiber based system providing additional polarization sensitive image contrast is available from Thorlabs Inc. (PSOCT-1300 Module, thorlabs.com). However, for this system no information on the polarization state of the sample beam is provided and it seems not to enable quantitative birefringence measurements. Therefore, to our knowledge, no single input state PS-OCT system, that provides quantitative polarization sensitive measurements, was published so far without any PM fibers or bulk polarizing components in the interferometer or detection unit.

In this work, we introduce a fiber based PS-OCT system featuring only conventional SM fibers in the interferometer and the detection unit. The use of a swept source with a central wavelength of 1040 nm provides fast imaging and deep penetration. Illuminating the sample with circular polarized light is provided by polarization control paddles in the sample arm while further paddles are used to achieve equal reference illumination power at the detector inputs and to control the polarization state throughout the fiber based system. We explain the polarization paddle arrangement and alignment sequence, which are key elements to the proper functionality of the system. Furthermore, we show results of calibration measurements and provide imaging results obtained in the macula and the nerve head area of healthy human volunteers.

2. Methods

2.1 Polarization sensitive single mode fiber based SS-OCT setup

Our system is based on a Mach-Zehnder interferometer. A sketch of the setup is shown in Fig. 1. Light from a swept source (SS, Axsun Technologies, sweep rate: 100 kHz, average sweep speed: 18 nm/μs) with a central wavelength of 1040 nm and a sweep range of 110 nm enters the input of a fiber based linear polarizer (LP). Polarization control paddles (PC, FPC030, Thorlabs Inc.) are used to set the illumination power at the sample by manipulating the polarization state before the polarizer. Linear polarized light enters fiber 1 of the first SM fiber based non-polarizing beam splitter, BS1 (50/50 (R/T)), where it is split into sample and

#210928 - $15.00 USD Received 2 May 2014; revised 24 Jun 2014; accepted 18 Jul 2014; published 28 Jul 2014

reference light. The light of the sample arm travels through fiber 2 of BS1 and a circular polarization state at the sample is achieved by adjusting PC1. After a galvo-scanner the light passes a scanning telescope with a focal length ratio of 75⁄50. The position of the second telescope lens can be shifted along its optical axis in order to compensate refractive errors of the eye. After being backscattered at the sample the light travels back to BS1 (via fiber 2 of BS1) and BS2 (via fiber 3 of BS1 and fiber 1 of BS2 (50⁄50 (R/T))). The output fiber 3 of BS1 and input fiber 1 of BS2 are directly linked to each other by a fiber connector. In the reference arm, the light travels along the output fiber 4 of BS1 and enters a free space section. This section is used to account for a mismatch in optical path length and dispersion between sample and reference arm. In order to compensate for the double pass through the BS1 fiber 2 in the sample arm section, an additional SM fiber is inserted into the reference arm. PC4 is adjusted in order to achieve equal reference power at the detector inputs (1.a, 1.b of PBS1 and 2.a, 2.b of PBS2). Both BS2 outputs are equipped with polarization control paddles (PC2 and PC3) and are connected to the inputs of PBS1 and PBS2. PC2 and PC3 are used in order to adjust the polarization state of the light entering PBS1 and PBS2 as described in the next section 2.2. The PBSs split the interfered light according to their polarization axis into a horizontal and a vertical polarization channel. At the detectors (Thorlabs, PDB 460C) the two corresponding signals are combined to obtain a balanced detection. The balanced signals are digitized using a dual channel digitizer (AlazarTech, Inc.) with 12 bit resolution at a frequency of 500 MHz.

In order to resample the signal to achieve equal spacing in k-space, an auxiliary common path interferometer was used to record a reference scan prior to OCT imaging. From this reference scan, nonlinearities of the sweep in k-space are determined, and the information is used to resample the OCT signals recorded thereafter.

2.2 Polarization state alignment

Like in our former work on PS-OCT we illuminate the sample with circular polarized light. This enables the measurement of backscattered intensity, retardation, and optic axis orientation simultaneously within a single A-scan [18]. Since SM fibers distort the polarization state of the light in an unpredictable way (depending on torsion, bending, etc.) the polarization state has to be carefully controlled by the polarization paddles. A proper alignment sequence for these paddles is a key to achieve correct functionality. The corresponding procedure to align the polarization for our novel SM fiber based SS-PS-OCT instrument is explained in the following.

Linear polarized light, output by the PM fiber of the polarizer, enters the SM fiber interferometer. Therefore, the fibers 1 plus 2 of BS1 have to mimic a quarter-wave-plate (QWP) in order to obtain circular polarized light at the sample. This can be achieved by aligning the paddles of PC1. We checked for the circularity of the polarization state at the sample position by rotating a linear polarizer mounted at the sample position and monitored the transmitted power. The power (integrated over the spectrum) was constant to within 2% during rotation of the polarizer by 360°, demonstrating a well-defined circular polarization state at the sample. In section 3, a further calibration experiment will be presented to demonstrate the circular state at the sample position. In a next step, PC2 and PC3 are aligned. For that purpose we block the reference arm and introduce a mirror in the sample arm to backreflect the light into the sample arm. For the backreflected light, the combination of the fibers 2 of BS1, 3 of BS1, 1 of BS2, 2 of BS2 (3 of BS2) and the input fiber 1.I (2.I) of PBS 1 (PBS2) have to work as a QWP. This means that, in absence of polarization alterations caused by the sample, circular polarized light reflected at the sample is converted into linear polarized light at the PBSs. In order to achieve this condition we adjust the paddles of PC2 (PC3) while monitoring the outputs of PBS1 (PBS2). This is done until a minimum is found at one output while a power maximum is present at the respective other output. The circular polarized light from the sample was transformed into a linear polarized state, being parallel to one of the polarization axes of the PBS, by the collective action of the fibers. The power ratio between the two outputs of PBS 1 (and 2), defining the linearity of the polarization state, was

#210928 - $15.00 USD Received 2 May 2014; revised 24 Jun 2014; accepted 18 Jul 2014; published 28 Jul 2014

measured to be 50:1. In a final step the polarization state of the reference light is adjusted to provide equal reference power in all 4 detector inputs. For that purpose, we block the sample arm and align the paddles of PC4 to achieve equal power at both outputs of PBS1 (PBS2).

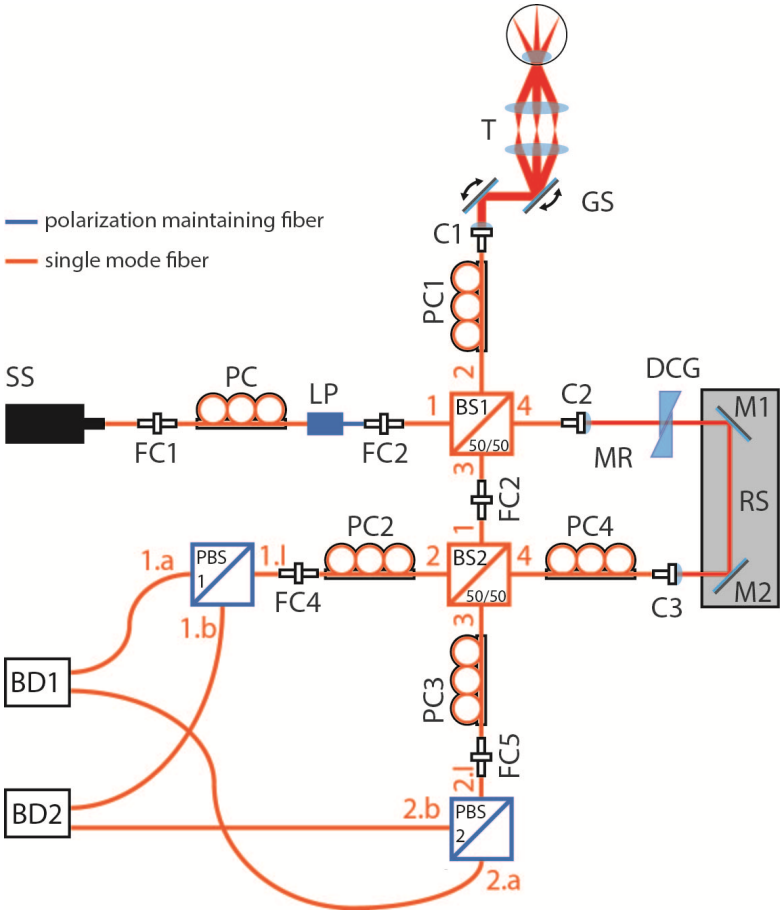

Fig. 1. Schematic diagram of the single mode fiber based SS-PS-OCT setup: SS, swept source; FC, fiber connector; PC, polarization controller; LP, linear polarizer; BS, beam splitter; C, collimator; GS, galvo scanner; T, Telescope; DCG, dispersion compensation glass; M, mirror; RS, reference stage; PBS, polarizing beam splitter; BD, balanced detector

The described procedure provides an SM fiber based PS-OCT system which has similar properties as previously reported bulk and PM-fiber based systems that also use a circular polarization state at the sample [18,36–38]. Accordingly, for light that has double passed the sample, reflectivity R, (single pass) phase retardation δ, and (relative) axis orientation θ, can be obtained as follows:

$$R(z) \sim A_1(z)^2 + A_2(z)^2 \tag{1}$$

$$\delta(z) = \arctan\left(\frac{A_2(z)}{A_1(z)}\right) \tag{2}$$

$$\theta = (180° - \Delta\varphi)/2 + \varphi_0 \tag{3}$$

where A_1 and A_2 are amplitudes as recorded by the two polarization channels, Δφ is the phase difference between the two channels at the same sample position, z is the depth coordinate

#210928 - $15.00 USD Received 2 May 2014; revised 24 Jun 2014; accepted 18 Jul 2014; published 28 Jul 2014

and φ_0 is an axis offset. It should be mentioned that Eqs. (2) and (3) are based on the assumption of a constant axis orientation with depth.

With an A-scan rate of 100 kHz and an illumination power of 2 mW we achieved a maximum sensitivity of 97.5 dB close to the zero delay. The roll off over 2 mm was measured to be 0.5 dB. The axial resolution in air was measured to be 9 µm. This setup provides various scan patterns and a maximum scan field of up to 40° × 40°. However, for the results presented in this paper we used a scan pattern of 1024 × 256 A-scans and a scan field of 25° × 25°.

2.3 Polarization sensitive data analysis

Polarization sensitive data evaluation was done according to concepts published in more detail elsewhere [18,36]. First we applied a series of standard FD-OCT post processing procedures (rescaling, zero padding, dispersion correction, inverse Fourier transformation and subtraction of the mean pattern). From the obtained amplitude and phase data we calculated reflectivity, retardation, optic axis orientation, Stokes vectors and degree of polarization uniformity (DOPU) [26].

For retinal imaging, additional post processing steps were performed: The polarization effects caused by the anterior eye segment birefringence were corrected by a software compensation algorithm [39].

RPE segmentation was performed according to DOPU values [26], which were calculated by Stokes vector analysis, within windows of 14 × 14 pixel (axial × lateral = 20 × 100 µm). Tissue showing DOPU values below a threshold of approximately 0.87 was classified as RPE. Both parameters, window size and threshold, were determined empirically according to the best visual impression. All evaluations for the different subjects were performed with the same window size and similar threshold values (0.85-0.90). In a next step 2D maps of retinal retardation and optical axis orientation were calculated [37]. In order to do so, light that has double passed the respective retinal layers, has to be evaluated. For this purpose we choose the signal backreflected from posterior retinal layers. Because of the strong reflectivity of the layers of the inner/outer photoreceptor segments junction (IS/OS junction) and the end tips of the photoreceptors (ETPR), they are well suited for this purpose. These layers are located directly anterior to the RPE. Using the RPE segmentation the anterior of the RPE can be found. Along each A-scan all retardation and axis orientation values within a band approximately 80 µm anterior to the RPE are averaged, thereby IS/OS junction and ETPR signals are considered exclusively. The respective averaged retardation and axis orientation values are then assigned to the corresponding transversal position. This yields 2D maps of retinal retardation and optical axis orientation.

3. Results

In order to show that the polarization alignment procedure of our fiber based PS-OCT setup is valid we performed measurements in a simple test sample of fixed retardance (rotatable wave plate). Furthermore we demonstrate the suitability of the system for in vivo retinal imaging on healthy human volunteers.

3.1 Measurements on a test sample

Based on our alignment procedure and according to theoretical considerations published elsewhere [18,35] retardation and axis orientation measurements should be independent of each other (also see Eq. (2) and (3)). As a test sample, we used a rotatable wave plate (retardation 67.5°), which we placed in front of a mirror into the sample arm. The retarder was rotated in steps of 10° for a total of 180°. At each orientation 16k A-scans were recorded. Retardation and axis orientation were obtained according to Eq. (2) and (3), the values were averaged and displayed versus the set retarder orientation.

Figure 2 shows that the measured retardation (blue triangles) remains nearly constant while the retarder orientation is changed. However, a slight modulation around the expected value (solid blue line) can be observed. The mean retardation value of all retarder orientations yields a value of 69.7° with a standard deviation of 1.4°. This is in good agreement with the

#210928 - $15.00 USD Received 2 May 2014; revised 24 Jun 2014; accepted 18 Jul 2014; published 28 Jul 2014

expected retardation of 67.5°. Furthermore a linear relation between measured and set axis orientation values (red squares) is observed. Subtraction of the axis orientation offset and unwrapping yields a linear increase of the axis from 0° to 180°, as expected (green squares). The agreement with expected values (solid green line) is excellent. Due to the observed offset the measured axis orientation has to be considered a relative axis orientation.

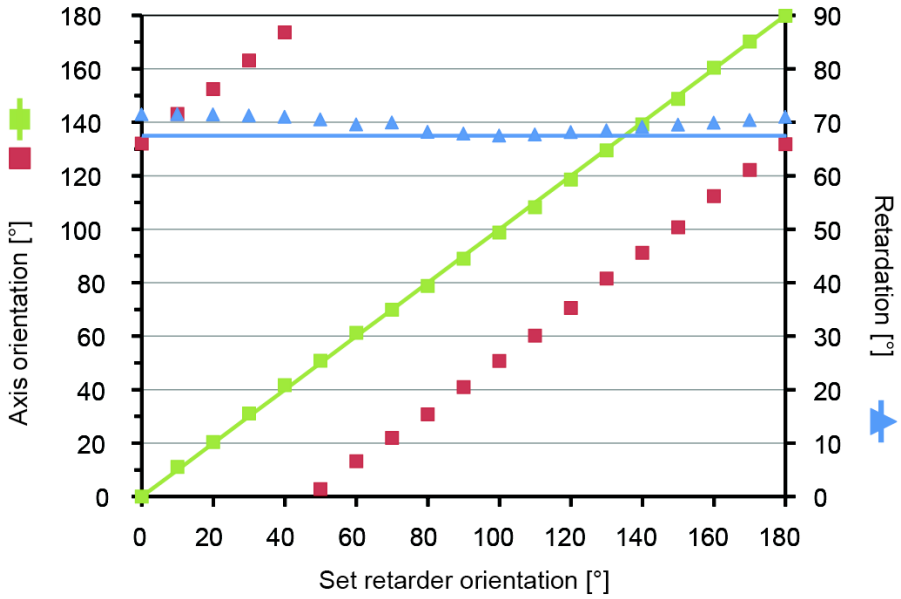

Fig. 2. Plot of measured axis orientation (scaled according to ordinate on the left) and retardation values (scaled according to ordinate on the right) versus set retarder orientation: averaged axis orientation values (red squares); unwrapped and offset subtracted axis orientation values (green squares); expected axis orientation values (solid green line); averaged retardation values (blue triangles); expected retardation values (solid blue line)

Since our setup uses conventional SM fibers, the polarization state stability of our system needs to be investigated. Fiber movement can lead to polarization state changes and thereby corrupt the measurement. In order to minimize these disturbances, SM fibers were placed into foam boxes and, where necessary, fixed to stable structures. These measures should minimize axis orientation or retardation drifts due to temperature changes or mechanical disturbances. To evaluate the stability of the setup, we performed repeated measurements on the test sample. The baseline was determined directly after alignment of the polarization paddles while two further measurements were performed 6 hours and 14 days after the alignment. The results are shown in Table 1. A maximum deviation of measured retardation of 4.4° was observed after 14 days with a standard deviation of 2°. The maximum change of axis offset was 3° while slope and range of axis orientation remained constant.

Tab. 1 Table of repeated measurement, baseline, 6 hours and 14 days after paddle alignment

time after paddle alignment	single pass retardation [°]		axis offset [°]	axis slope [-]
	mean	SD		
baseline	**66.9**	**1.6**	**132.1**	**0.99**
6 h	**66.5**	**1.5**	**129.1**	**1.01**
14 d	**70.9**	**2**	**131.6**	**1.00**

#210928 - $15.00 USD Received 2 May 2014; revised 24 Jun 2014; accepted 18 Jul 2014; published 28 Jul 2014

3.2 Measurements in human retina

To demonstrate the full functionality of our novel SM fiber based SS-PS-OCT system for in vivo retinal imaging we performed measurements in the macula and the nerve head region of healthy human volunteers. Three-dimensional data sets were acquired and evaluated according to the procedure described in section 2.3. Before the measurement full informed consent was obtained from all volunteers. The ethics committee of the Medical University of Vienna approved all measurements following the tenets of the Declaration of Helsinki.

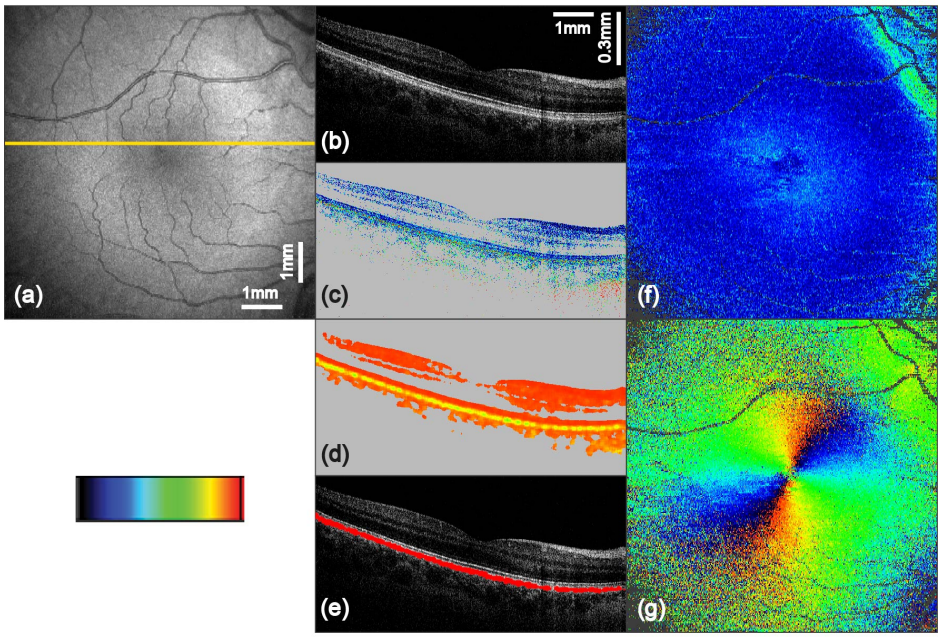

Fig. 3. PS-OCT imaging results of the macula region from a healthy human volunteer (scan angle 25° × 25°, scan pattern 1024 × 256 A-scans). The yellow line in (a) indicates the position of the corresponding B-scans in (b) to (e): (a) fundus projection image; (b) intensity B-scan on logarithmic gray scale; (c) retardation image (color scale 0° to 30°); (d) DOPU image (color scale 0 to 1); (e) overlay of segmented depolarizing structures (red) with the intensity image; (f) 2D en face retardation map retrieved at IS/OS and ETPR (color scale 0° to 30°); (g) 2D en face axis orientation map retrieved at IS/OS and ETPR (color scale −90° to + 90°)

During measurements a movable headrest is used to align the head of the volunteer while a fixation target is displayed to the contralateral eye. Monitoring of the beam position is done with a CCD pupil camera. At an A-scan rate of 100 kHz we used an illumination power of 2 mW at the cornea, which is within the laser safety limits for a scanning beam in this wavelength region [40,41].

Figures 3 and 4 show exemplary sets of retinal en face images and B-scans as measured with our instrument. The yellow line in the fundus projection image (Fig. 3(a) and Fig. 4(a)) indicates the position of the corresponding B-scans.

Figure 3(a) provides an overview of the scanned region of the retina around the macula. In the tomographic intensity image, Fig. 3(b), the four posterior layers (external limiting membrane (ELM), IS/OS, ETPR and RPE) can be distinguished. While the posterior three of these layers show approximately similar reflectivity, additional contrast is provided in the cornea compensated retardation image, Fig. 3(c). In this image the RPE clearly changes the polarization state of the backscattered light while this is not the case for the other layers. By computing DOPU values the depolarizing nature of the RPE can be displayed in an even more

#210928 - $15.00 USD Received 2 May 2014; revised 24 Jun 2014; accepted 18 Jul 2014; published 28 Jul 2014

pronounced way, Fig. 3(d). The mean DOPU value in the RPE was 0.81 (range: 0.60 – 0.87) while the inner retinal layers showed a mean value of 0.96 (range: 0.87 – 0.99). By extracting pixels with a DOPU value lower than 0.87, indicating depolarizing tissue, the RPE can be segmented. Figure 3(e) shows the extracted low DOPU values in red, overlaid with the respective intensity image. 2D maps of retardation and axis orientation measured at the level of the photoreceptors are presented in Fig. 3(f) and 3(g). In the foveal region of (f) the doughnut shaped retardation pattern caused by Henle's fiber layer can be observed [42]. Furthermore elevated retardation values can be seen superior and inferior of the nasal region on the right. These effects are caused by the nerve fiber bundles spreading from the optic nerve [43]. In Fig. 3(g) the radial pattern of the axis orientation can be observed which is also caused by the Henle fibers [42].

Figure 4 shows a further set of en face images and B-scans taken from another volunteer, showing the area around the optic disc. Similar to the first set of images, the cornea compensated retardation image, Fig. 4(c), provides additional image contrast and information. In the center of this image an increase of retardation with depth (from blue to green colors) can be observed in the thick part of the RNFL (topmost bright layer in the intensity image Fig. 4(b)). The extraction of low DOPU values from Fig. 4(d) yield a satisfying image in the overlay with the intensity B-scan in Fig. 4(e). Occasionally slight depolarization was observed in the areas beneath larger blood vessels of the retina and in parts of the choroid which is also slightly pigmented. RPE segmentation errors caused by such effects can be handled by more sophisticated algorithms [44]. Furthermore the B-scans show a good penetration depth, enabling the visualization of the junction between choroid and sclera (see white arrows in Fig. 4(b)). The retardation map displayed in Fig. 4(f) shows increased retardation values in the superior and inferior region around the optic nerve head which are caused by the thick nerve fiber bundles of the RNFL layer in these areas. Moreover, thin nerve fiber bundles and their spreading along the major blood vessels can be observed. Figure 4(g) displays the RNFL axis orientation en face map. The approximately radial distribution pattern of the axis orientation values is caused by the nerve fiber bundle distribution which radiate from the optic disc [43,45].

Retardation and DOPU B-scan images were intensity thresholded in order to exclude noisy areas whose polarization states are unreliable. Excluded pixels appear in grey. For all of the displayed 2D en face maps blood vessels and areas with low signal quality (mainly at the corners of the images and at the nerve head) are displayed in dark grey. The results obtained by polarization sensitive evaluation of data collected in the retina with our novel SM fiber based SS-PS-OCT setup, as shown in Fig. 3 and 4, are in good agreement with work that was published previously [23,24,42,46].

#210928 - $15.00 USD Received 2 May 2014; revised 24 Jun 2014; accepted 18 Jul 2014; published 28 Jul 2014

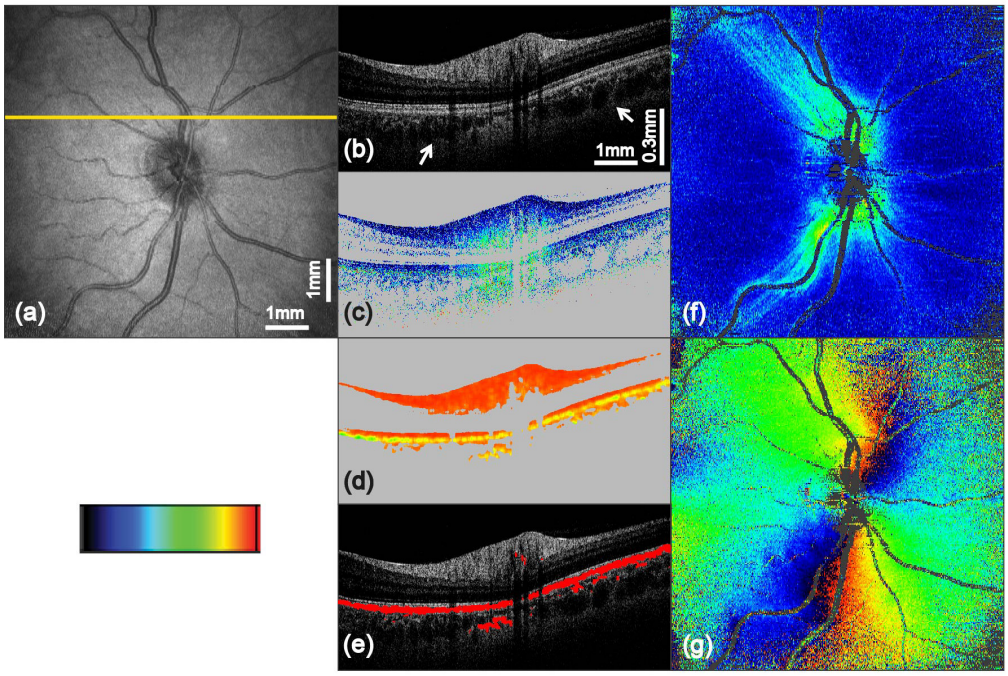

Fig. 4. PS-OCT imaging results of the optic disc region from a healthy human volunteer (scan angle 25° × 25°, scan pattern 1024 × 256 A-scans). The yellow line in (a) indicates the position of the corresponding B-scans in (b) to (e): (a) fundus projection image; (b) intensity B-scan on logarithmic gray scale; (c) retardation image (color scale 0° to 40°); (d) DOPU image (color scale 0 to 1); (e) overlay of segmented depolarizing structures (red) with the intensity image; (f) 2D en face retardation map retrieved at IS/OS and ETPR (color scale 0° to 40°); (g) 2D en face axis orientation map retrieved at IS/OS and ETPR (color scale −90° to + 90°)

4. Discussion and conclusion

We developed a new SS-PS-OCT system built with conventional SM fibers in the interferometer and detection unit. The only remaining PM fiber in our setup is located between the light source and the SM fiber based interferometer. It forms the output of a fiber based linear polarizer, which, in combination with a polarization controller before the polarizer, is used as a convenient means of illumination power regulation at the sample. However, by using another method for power control, this PM fiber could be omitted. The use of conventional SM fibers in the interferometer and detection part avoids long PM fibers. Polarization paddles are used to set a circular polarization state for the sample illumination, to handle the polarization state throughout the system, and to provide equal reference power at the detector inputs. Aligning the polarization state with the polarization paddles needs little additional equipment, is reliable and can be completed in less than 30 minutes. Measurements in a test sample (wave plate) proved that retardation measurements and optical axis orientation measurements are independent of each other. This indicates that our polarization state alignment procedure works well. Moreover, this demonstrates the correct adjustment of polarization states throughout the SM fiber system and that the application of the respective equations to calculate retardation and axis orientation is justified. The observed results show low deviations from expected values which are in the same range as reported previously with bulk optics and PM fiber based systems [18,35]. Furthermore, repeated measurements over extended time periods demonstrate that our system is rather stable over time with respect to the set polarization states. For the measurements of axis orientation we observed an offset. The reason for this might be the unknown reference beam polarization state at the polarizing beam splitters. Deviations from a linear state oriented at 45° will introduce a phase offset,

#210928 - $15.00 USD Received 2 May 2014; revised 24 Jun 2014; accepted 18 Jul 2014; published 28 Jul 2014

associated with a corresponding axis offset. Therefore, the measured axis orientation is a relative value, i.e. consistent within a data set but not an absolute value with respect to the instrument coordinate frame. If absolute values of axis orientation are required, this axis offset can be accounted for by a calibration measurement. The remaining very slow retardation drift of the order of 1-2° per week might be further reduced by improved shielding of the SM fibers against environmental disturbances which also seems advisable for the use in a clinical setting.

In vivo retinal measurements on healthy human volunteers nicely correlate with work that has been published before. Compared to PS-OCT at 840 nm improved penetration depth was achieved. Polarization changing tissues like the depolarizing RPE [25,45], or the birefringent RNFL [43,45] were identified and imaged with high quality. Using DOPU values in order to segment the RPE also showed satisfying results. Birefringence of Henle fibers can be observed in the retardation and axis orientation en face maps of the macula region [42,45]. The doughnut shaped retardation pattern of Henle's fiber layer with its radial distribution of axis orientation values was clearly observed. In the optic nerve head area the computed en face maps of retardation and axis orientation show the spreading of nerve fiber bundles in high detail as well as the radially symmetric distribution of axis orientation values [37,43]. The observed 6h drift of measured retardation during the stability measurements of 0.4° (SD = 1.6°) is low compared to typical retardation values of up to 12° in the macula and 30° in the optic disc area. However, the retardation drift after 14 days of 4.0° (SD = 2.0°) suggests either improved shielding against environmental disturbances, a more frequent alignment check or numerical correction.

Recently another fiber based single input state PS-OCT setup, partially built with SM fibers was reported [35]. This system is equipped with SM fibers spliced to sample and reference arm PM fibers of a BS. Polarization controllers along these SM fibers are adjusted to mimic QWPs and therefore enable to avoid any bulk optics wave plates, paving the way to endoscopic applications. However, a substantial part of the interferometer unit and the entire detection unit of that system still uses PM fibers and PM fiber components.

To summarize, we presented, to the best of our knowledge, the first PS-OCT system that uses a singular circular polarization state at the sample, featuring exclusively conventional SM fibers in both, interferometer and detection unit. Nonetheless it shows all advantages for in vivo retinal imaging that a fiber based PS-OCT systems using a swept source at 1040 nm can provide.

Acknowledgments

The authors wish to thank H. Sattmann from the Center for Medical Physics and Biomedical Engineering for technical assistance.

#210928 - $15.00 USD Received 2 May 2014; revised 24 Jun 2014; accepted 18 Jul 2014; published 28 Jul 2014